# 3D Printed Polycaprolactone Carbon Nanotube Composite Scaffolds for Cardiac Tissue Engineering

Chee Meng Benjamin Ho, Abhinay Mishra, Pearlyn Teo Pei Lin,
Sum Huan Ng, Wai Yee Yeong, Young-Jin Kim,* Yong-Jin Yoon*

Fabrication of tissue engineering scaffolds with the use of novel 3D printing has gained lot of attention, however systematic investigation of biomaterials for 3D printing have not been widely explored. In this report, well-defined structures of polycaprolactone (PCL) and PCL-carbon nanotube (PCL-CNT) composite scaffolds have been designed and fabricated using a 3D printer. Conditions for 3D printing has been optimized while the effects of varying CNT percentages with PCL matrix on the thermal, mechanical and biological properties of the printed scaffolds are studied. Raman spectroscopy is used to characterise the functionalized CNTs and its interactions with PCL matrix. Mechanical properties of the composites are characterised using nanoindentation. Maximum peak load, elastic modulus and hardness increases with increasing CNT content. Differential scanning calorimetry (DSC) studies reveal the thermal and crystalline behaviour of PCL and its CNT composites. Biodegradation studies are performed in Pseudomonas Lipase enzymatic media, showing its specificity and effect on degradation rate. Cell imaging and viability studies of H9c2 cells from rat origin on the scaffolds are performed using fluorescence imaging and MTT assay, respectively. PCL and its CNT composites are able to show cell proliferation and have the potential to be used in cardiac tissue engineering.
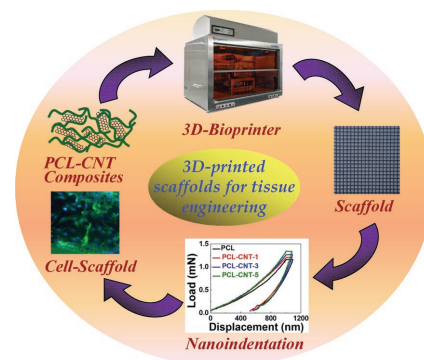
C. M. B. Ho, Dr. A. Mishra, P. T. P. Lin, Prof. W. Y. Yeong,
Prof. Y.-J. Kim, Prof. Y.-J. Yoon
School of Mechanical and Aerospace Engineering
Nanyang Technological University
50 Nanyang Avenue 639798, Singapore
E-mail: yj.kim@ntu.edu.sg; yongjiny@ntu.edu.sg
C. M. B. Ho, Dr. A. Mishra, Prof. W. Y. Yeong,
Prof. Y.-J. Kim, Prof. Y.-J. Yoon
Singapore Centre for 3D Printing
Nanyang Technological University
50 Nanyang Avenue 639798, Singapore
C. M. B. Ho, Dr. S. H. Ng
A*STAR's Singapore Institute of Manufacturing
Technology (SIMTech)
2 Fusionopolis Way, Level 10 Innovis and Kinesis, 138634
Singapore

1. Introduction

Tissue engineering is defined as an interdisciplinary field which involves the use of cells and a scaffold/matrix to develop new functional tissue for implantation back to the donor.[1,2] 3D scaffolds play a vital role in tissue engineering as they are commonly used for drug delivery, investigation of cell behavior, and material.[3] Moreover, the scaffold should essentially provide a biological environment in which cells can readily attach, proliferate, and maintain their differentiated phenotype and allow deposits of new tissue matrix throughout the entire construct.[4,5]

Polymeric biomaterials such as polyurethane (PU), polylactic acid, polycaprolactone (PCL), and poly(L-lactide-co-ε-caprolactone) have attracted significant interest due to

wileyonlinelibrary.com
1

their unique mechanical, biocompatible, biodegradable, and nontoxic properties.[6–11] In recent years, PCL-based biomaterials have been extensively used in biomedical, pharmaceutical, controlled drug delivery, and tissue engineering applications.[12–16] Although biocompatibility, biodegradability, mechanical, and structural stability are some well-known properties of PCL, its lack of bioactivity and surface energy (high hydrophobicity) have led to reduced cell affinity and small tissue regeneration rates.[17] One of the strategies to reduce these limitations is to use nanocomposites of nanoclay,[18] graphene,[19] or carbon nanotube (CNT).[20–22]

The incorporation of reinforcing agent such as nanoparticles in the polymer matrix further stimulates the thermomechanical and biological response.[23–25] Multiwalled CNT (MWCNT) possesses exceptional mechanical, electrical, and optical properties. Its high aspect ratio structure makes it useful as a nanofiller in the fabrication of polymeric nanocomposites, possibly leading to improved mechanical properties, biocompatibility, and reduced cytotoxic effect for biological applications.[26] The regenerative capabilities of the adult human myocardium when compared to the blood or skin are significantly minimal and insufficient to compensate for the loss of cardiac myocytes. A combination of the right cells, matrix, molecular and physical regulatory factors have to be present in order to induce tissue development and remodeling of the myocytes.[27,28]

PCL nanocomposites (nanoclays, graphene, and CNTs) can be prepared using methods such as solvent casting, freeze drying, and electrospinning.[19,21,22,29–34] However, these existing fabrication methods are unable to produce scaffolds of desired control pore sizes. Recently, research groups have started looking into the use of 3D printing applied to the field of biology.[35–38] In 3D printing, models are designed on computer-aided design (CAD) software or obtained through a computerized tomography (CT)/magnetic resonance imaging (MRI) scan which is then converted to a Stereolithography (STL) file. The STL file consists of a series of 2D cross-sectional layers, creating a path for the printer to take for tracing.[36] This layer-by-layer approach has the ability to generate spatially controlled cell patterns, fabricates complex geometry scaffold and printing of multimaterials. These advantages give 3D printing its newly acquired popularity.[39–42]

In this work, we focus on the printing of PCL and CNT in conjunction with the 3D printer. Scaffolds with well-defined structure have been successfully designed and fabricated using a 3D printer. The improved thermal and mechanical properties of printed scaffolds with various percentages of CNTs have been reported. The biodegradation behavior of PCL and its CNT composites have been examined in enzymatic media. Furthermore, cytotoxicity and cell compatibility of PCL-CNT composites have also been studied.

2. Experimental Section

2.1. Materials

PCL (M_n = 80 000) was purchased from Sigma-Aldrich. Functionalized MWCNTs (20–30 nm outer diameter, 5–10 nm inner diameter with 10–30 μm length) were purchased from Chengdu Organic Chemicals Co., China. Chloroform, 3-(4,5-dimethylthiazol-2-yl)-2,5-diphenyltetrazolium bromide (MTT), and other chemicals were purchased from Sigma-Aldrich.

Cardiac H9c2 cells of rat origin were derived from the same initial CRL-1446 cell culture obtained from the American type culture collection. Cells were maintained in Dulbecco's modified Eagle's medium (DMEM) (SH30243.02, HyClone, GE Healthcare) supplemented with 10% fetal bovine serum (F1051 Sigma-Aldrich), 1% Penicillin-Streptomycin (P4333 Sigma-Aldrich), and grown at 37 °C in a 5% CO_2 humid atmosphere.

2.2. Nanocomposite Preparation

The nanocomposites were prepared by adding well dispersed CNT solution and PCL in chloroform, the mixture is then sonicated. Different amounts (1%, 3%, and 5%) of CNTs were determined according to w/w% of PCL and sonicated (Model 505 Sonic Dismembrator from Fischer Scientific) with predetermined volume of chloroform for 10 min. The well-dispersed CNT solution in chloroform was mixed in PCL with chloroform solution and sonicated for 30 min. The PCL/chloroform ratio was kept constant to 8% (w/v). Pure PCL (8% w/v) was also dissolved in chloroform and sonicated for 30 min. Hereafter, we will term the nanocomposites as PCL-CNT-1, PCL-CNT-3, and PCL-CNT-5 using 1%, 3%, and 5% CNT as the nanofiller, respectively.

2.3. 3D Printing of PCL and PCL-CNT Scaffolds

PCL and its nanocomposites were fabricated and printed by *RegenHU Bioprinter Biofactory Machine (Switzerland)*. A grid structure was designed using BioCad software. The structure covering 20 mm × 20 mm consisted of two horizontal and two vertical lines separated by 1 mm.

PCL and its nanocomposites solution were charged into two 5 mL syringes, which were then connected to a gauge 21 nozzle tip and the dispenser. The substrate for printing the biomaterial can be fixed on the stage by turning on the vacuum selection. The pressure of the 3D printer was first set to 1 bar for extrusion of the PCL and was tuned for the systematic free flow of loaded material (nanocomposite) accordingly. The syringes containing the 8% PCL solution or with its nanocomposites were connected to the nozzle and calibration with the needle length measurement (NLM) testing (distance between the needle and the glass slide) was done before dispensing any solution out of the syringe. For this bioprinting system, the feed rate refers to the speed in which the stage moves (*x*, *y*-direction) allowing for the material to be deposited while the thickness refers to the stage moving in the *z*-direction after each layer is printed. As the feed rate of the 3D printer is an important parameter for printing well-defined patterns, feed rate values of 800, 1000, and 1200 were used while keeping the other variables constant. Several batches of PCL and

www.MaterialsViews.com

Early View Publication; these are NOT the final page numbers, use DOI for citation !!

its nanocomposites were printed using an optimized feed rate. The PCL and its nanocomposite grid scaffolds were dried under vacuum for 24 h before performing any characterization or testing. Microscopic images of the scaffolds were captured using stereo microscopes (Olympus SZX7 and Zeiss Axiotech).

2.4. Enzyme Degradation

The enzymatic degradation of PCL and its CNT nanocomposite scaffolds was performed at 37 °C in potassium phosphate buffer solution (PBS) (pH 7.4) by Pseudomonas lipase (type XIII).[52] Scaffolds having dimensions of $5 \times 5 \times 0.15$ mm^3 were placed in a small tube containing 0.1 mg mL^{-1} Pseudomonas lipase with 3 mL of PBS. Enzymatic reaction was carried out for 3, 6, and 24 h after incubating the tubes at 37 °C with continuous shaking. The scaffolds were then washed with phosphate buffer and dried in vacuum oven. Scanning electron microscope (SEM) images before and after enzymatic degradation were captured by using JEOL JEM-5600LV scanning electron microscope.

2.5. Thermal Characterization

Differential scanning calorimeter (DSC) TA-DSC-Q-200 was used to measure the melting and crystallization temperatures along with the heat of fusion and crystallization of the scaffold materials. All the samples were heated and cooled at a scan rate of 10 °C min^{-1} in the first run to obtain the peak temperatures and enthalpies. A repeat second heating run was carried out.

2.6. Raman Spectroscopy

Raman spectroscopic measurements were carried out in back-scattering geometry using an Ar$^+$ excitation source of 514 nm wavelength coupled with a Renishaw inVia Raman microscope.

2.7. Nanoindentation

Nanoscale mechanical properties of PCL, PCL-CNT-1, PCL-CNT-3, and PCL-CNT-5 nanocomposites were studied using a nanoindenter (NanoTest Micromaterials Ltd, Wrexham, UK) with a 150 nm Berkovich pyramidal tip. The elastic modulus (E), maximum load, and hardness were obtained. Each sample was indented more than five times at different regions separated by a few millimeters.

2.8. Conductivity

Conductivity of PCL-CNT nanocomposites was studied by using Loresta-GP MCP-T600 from Mitsubishi Chemical Analytech.

2.9. Cytotoxicity and MTT Assay

Cell viability test with the scaffold materials was done using the Vybrant MTT Cell Proliferation Assay Kit by Thermofisher with a few modifications. Briefly, 50 000 cells were seeded onto the scaffold and placed into a 24-well plate with 1 mL of medium. After 4 d of cell seeding, the spent media was removed and 400 µL fresh medium and 40 µL MTT solution (component A) were added to each well. After 4 h incubation at 37 °C in 5% CO$_2$, MTT solution from each well was carefully removed. Instead of using Component B from the kit, 250 µL dimethyl sulfoxide was added to each well. The absorbance of solution was then measured at 540 nm using the TECAN Infinite 200 PRO plate reader.

2.10. Fluorescence Staining

Cells seeded on the PCL and PCL nanocomposite scaffolds were grown in DMEM media for 4 d. The scaffolds were washed two times with PBS and fixed with 4% paraformaldehyde for 15 min at room temperature. After washing off the paraformaldehyde, 0.1% triton X was added for 5 min. Scaffolds were then incubated for 30 min at room temperature with ActinGreen 488 Ready-Probes Reagent and NucBlue Fixed Cell ReadyProbes Reagent from Thermofisher Scientific for staining F-actin and the cell nucleus, respectively. After three washes with PBS, the scaffolds were transferred onto a glass slide where the images were captured by a Zeiss Axio fluorescence microscope.

2.11. Cell Viability and Immunofluorescence

To evaluate cell viability with the pure PCL and PCL-CNT nanocomposite, the live/dead viability/cytotoxicity kit for mammalian cells (Cat no L3224) from ThermoFisher scientific was used. H9c2 cells (≈50 000) were grown together with PCL and PCL nanocomposite in DMEM media for 4 d in a 24 well plate. After 4 d, the wells were washed twice with PBS followed by the addition of 200 µL of 2×10^{-6} M Calcein AM and 4×10^{-6} M EthD-1 solutions from the kit in the wells and incubated for 30 min at 37 °C. Zeiss Axio fluorescence microscope was used to observe the cells inside the wells.

2.12. Statistical Analysis

Data are presented as the mean ± standard deviation compared using unpaired t-test. All data were analyzed using Prism software (version 6.01). $P < 0.05$ was considered to indicate a statistically significant difference.

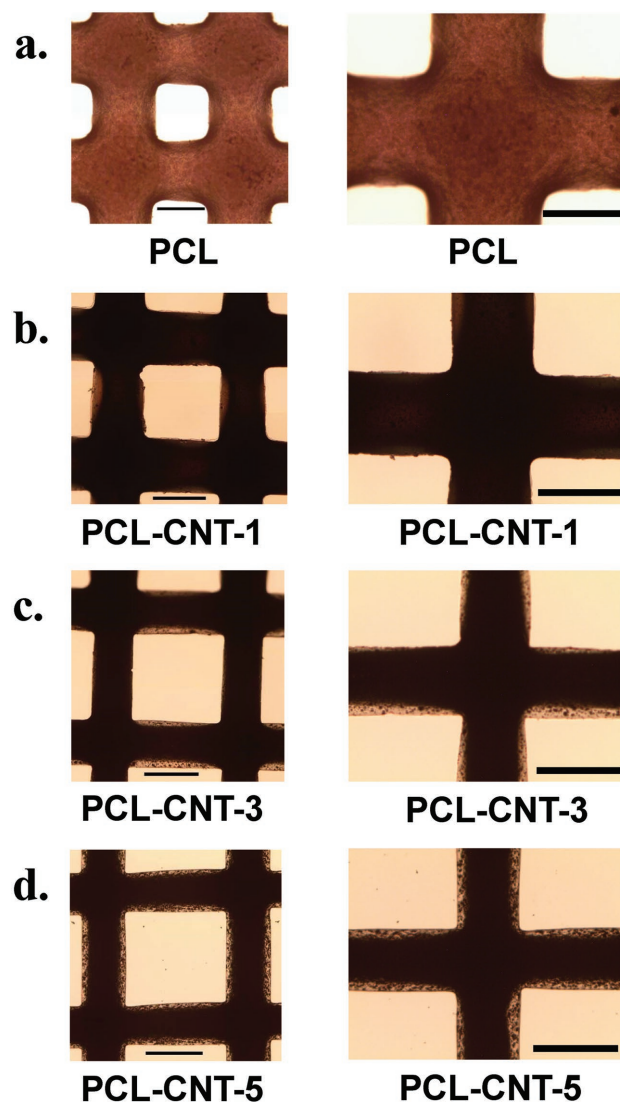## 3. Results and Discussion

3.1. 3D Printing of Scaffolds

Figure 1a shows the images of the 3D printed scaffolds of PCL and its nanocomposites. Conditions for 3D printing have been achieved by changing the pressure, speed (feed rate), and needle size. Optimized conditions for different feed rates with constant temperature, pressure, and needle size have been compiled in Table S1 (Supporting Information). Printed PCL and its CNT composite scaffolds with different feed rates have been compiled in Figure S1 (Supporting Information). The default feed rate and thickness were optimized at 1000 and 0.20 µm, respectively, for our further studies. The grid structure of the PCL and its

a.

PCL   PCL-CNT-1

PCL-CNT-3   PCL-CNT-5

b.
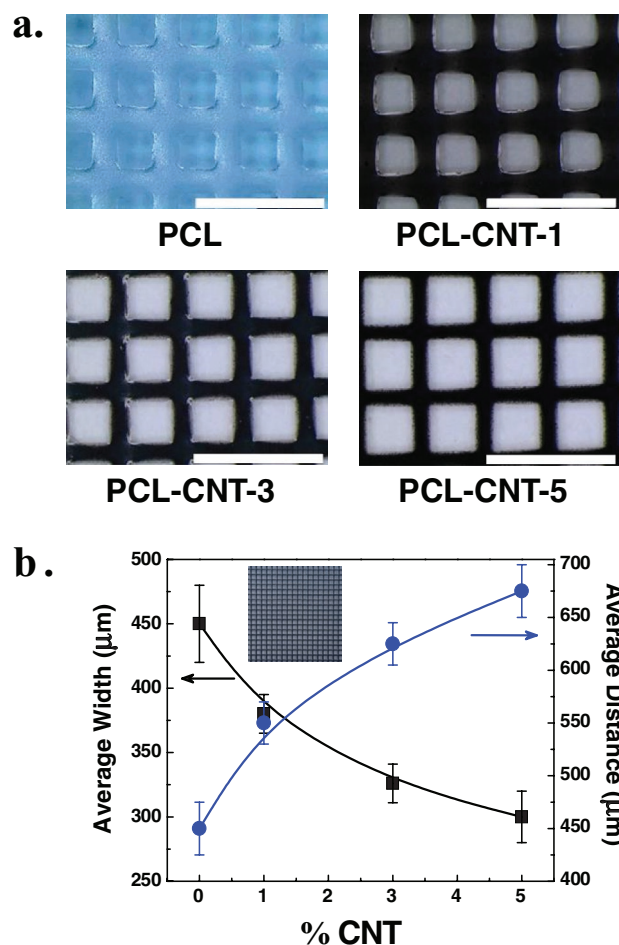
Figure 1. a) Stereo microscopic images of PCL and its nanocomposites (scale bar: 2 mm). b) Average line width of the grid (black squares) and average distance between the strips (blue circles) of PCL and its nanocomposites w.r.t. percentage of CNT present in the sample (inset figure showing the representative printed picture of PCL-CNT-5 scaffold).

a.

PCL   PCL

b.

PCL-CNT-1   PCL-CNT-1

c.

PCL-CNT-3   PCL-CNT-3

d.

PCL-CNT-5   PCL-CNT-5

Figure 2. Optical images of single window and cross junction of 3D printed pure PCL and its indicated nanocomposite grids: a) PCL, b) PCL-CNT-1, c) PCL-CNT-3, and d) PCL-CNT-5 (scale bar: 400 μm).

nanocomposites becomes more prominent with increasing CNT percentage. The nanotube and PCL matrix interaction plays a vital key role; CNT acts as a nanofiller and holds the PCL matrix to obtain the well-defined structures. Strip width decreases from PCL to PCL-CNT-5.

In order to obtain the detailed information of the printed scaffolds, the single window is being observed along with a grid through a bright field microscope. Moreover, several areas have been chosen in the scaffold to get the overall idea of the structure of the printed scaffolds. It is clearly observed from the images in Figure 2, as the nanoparticle percentage increases in the PCL matrix, the scaffold structure becomes more defined and ordered. The average width of PCL and its nanocomposites were determined by analyzing the images through high-frequency NBS 1963A standard resolution test target (R2L2S1P1) from Thorlabs (2″ x 2″) and toup camera software.

Figure 1b shows the graph between the average widths calculated versus the CNT percentage in the samples. The average strip widths of the PCL, PCL-CNT-1, PCL-CNT-3, and PCL-CNT-5 grid are 450 ± 30, 380 ± 15, 326 ± 15, and 300 ± 20 μm, respectively. The distance between each horizontal and vertical stripes of the grid window increases with increasing content of CNTs. The distance between horizontal and vertical strips of the PCL, PCL-CNT-1, PCL-CNT-3, and PCL-CNT-5 grid window are 425 ± 25, 550 ± 20, 625 ± 20, and 675 ± 25 μm, respectively (Figure 1b). The cross-junction of the grid also describes the prominent microstructure of the scaffolds. The inset of the Figure 1b shows the representative printed PCL-CNT-5 scaffold, as it is discernible from the image that the overall scaffold structure (length, breadth) is printed in a consistent manner with high precision.

www.MaterialsViews.com

Early View Publication; these are NOT the final page numbers, use DOI for citation !!

3.2. Characterization of 3D Printed PCL Nanocomposites

Raman spectroscopic technique is being used to observe the structural integrity of CNT in the PCL matrix. Figure 3 shows the Raman spectra of COOH functionalized CNT and their subsequent PCL nanocomposites (PCL-CNT-1, PCL-CNT-3, and PCL-CNT-5). The disordered graphite structure or sp^3-hybridized carbons of the CNT is demarcated by the peak at 1350 cm^{-1} also known as D-band, while the structural intensity of sp^2-hybridized carbon atoms or tangential mode is assigned to peak at 1580 cm^{-1} (G-band). The Raman spectrum of PCL shows the characteristic peaks at 1723 cm^{-1} (νC=O), 1040–1106 cm^{-1} (skeletal vibration), 1470–1415 cm^{-1} (δCH$_2$), and 1281–1305 cm^{-1} (wCH$_2$) attributable to CH$_2$ groups.[34,43,44] Both characteristic bands (D and G) are absent in pure PCL. The PCL characteristic peaks are also discernible in the nanocomposites. As the CNT content increases in nanocomposites, the peaks attributed to CH$_2$ groups and skeletal vibration becomes broad due to submerging of D band and the interaction of CNT's with PCL matrix.

There is no shifting of both D and G bands after nanocomposite formation, implying only physical adsorption of PCL on the surface of CNT. The degree of functionalization of CNTs can be estimated by the D–G band intensity ratio (I_D/I_G). The I_D/I_G ratio is calculated for CNT and its nanocomposites. The D band is merged with CH$_2$ group peaks of the PCL in its nanocomposites. The peaks in the range of 1200–1520 cm^{-1} have been deconvoluted and
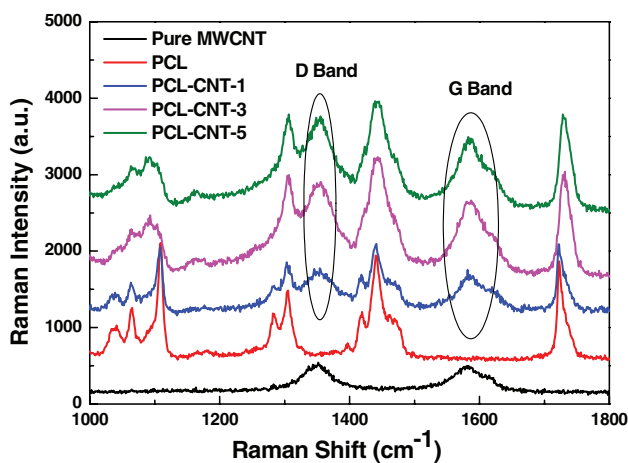
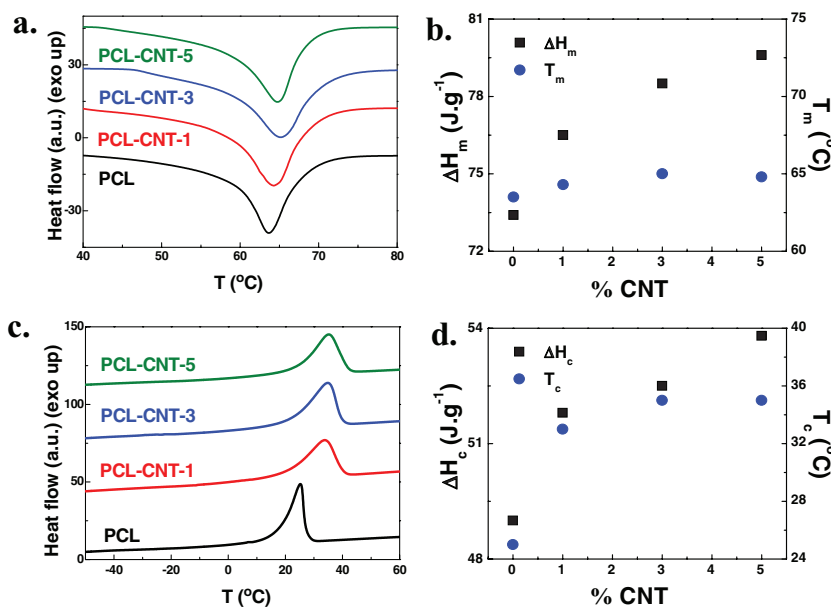*Figure 4.* DSC thermograms of PCL and its indicated nanocomposites: a) heating curves, b) graph representing the change heat of fusion (J g^{-1}) and melting temperature w.r.t. CNT percentage, c) cooling curves, and d) graph representing the change heat of crystallization (J g^{-1}) and melting temperature w.r.t. CNT percentage in the sample.

curve fitted. There was no significant change observed in I_D/I_G ratio for CNT and its nanocomposites, referring a physical adsorption of PCL onto CNT walls in the nanocomposites. Moreover, the structural integrity of CNT walls was totally conserved after the formation of nanocomposites.

3.3. Thermal Behavior

Figure 4a shows the representative DSC traces of PCL and its CNT nanocomposites. Distinct endothermic melting peaks (T_m) at 63.5, 64.3, 65, and 64.8 °C for PCL, PCL-CNT-1, PCL-CNT-3, and PCL-CNT-5, respectively, were observed. Heat of fusion (ΔH) increases in nanocomposites in the presence of CNTs (73.4, 76.5, 78.5, and 79.6 J g^{-1} for PCL, PCL-CNT-1, PCL-CNT-3, and PCL-CNT-5, respectively) due to enhanced interaction between polymer chains and CNTs (Figure 4b). The enhancement in the enthalpy of fusion is probably due to the nucleation effect of CNTs. The peak temperature and enthalpy of fusion for the second run has been compiled in Figure S2 (Supporting Information) shows the same behavior as the 1st run. The cooling curves reveal an increase in crystallization temperature (T_c) for nanocomposites as compared to pure PCL. The crystallization peaks are slightly broader for nanocomposites as compared to pure PCL (Figure 4c). The gradual shifting of T_c is being noticed from 25, 33, 35, and 35 °C for PCL, PCL-CNT-1, PCL-CNT-3, and PCL-CNT-5, respectively, and nanocomposites also seem to be slightly crystalline in cooling period as compared to pure PCL ((ΔH_c) 49, 51.8, 52.5, and 53.8 J g^{-1} for

Figure 3. Raman spectra of pure MWCNT, PCL, and its indicated nanocomposites.

Materials
Views
www.MaterialsViews.com

Macromol. Biosci. **2016**, DOI: 10.1002/mabi.201600250
© 2016 WILEY-VCH Verlag GmbH & Co. KGaA, Weinheim

Macromolecular
Journals

5

Early View Publication; these are NOT the final page numbers, use DOI for citation !!

PCL, PCL-CNT-1, PCL-CNT-3, and PCL-CNT-5, respectively) (Figure 4d). This is presumably due to the nucleating effect of CNT on PCL crystallization. Moreover, increase in the crystallization is also noticed for other polymers like PU due to the alignment of chains in the domains, due to self-assembly and increasing hard segment content.[45] Similarly, polymer chains may also align due to nucleation effect of CNTs, which increases the crystallization behavior of nanocomposites.[32,46] The increasing content of CNTs further increases the crystallization temperature and broadens the crystallization peak, indicating restricted mobility of polymer chains in the nanocomposite.

3.4. Nanoindentation (Mechanical Response of Scaffolds) and Conductivity

Figure 5a shows the load versus indentation depth representative curve for PCL and its nanocomposites obtained through nanoindentation.[47–49] The indentation depth
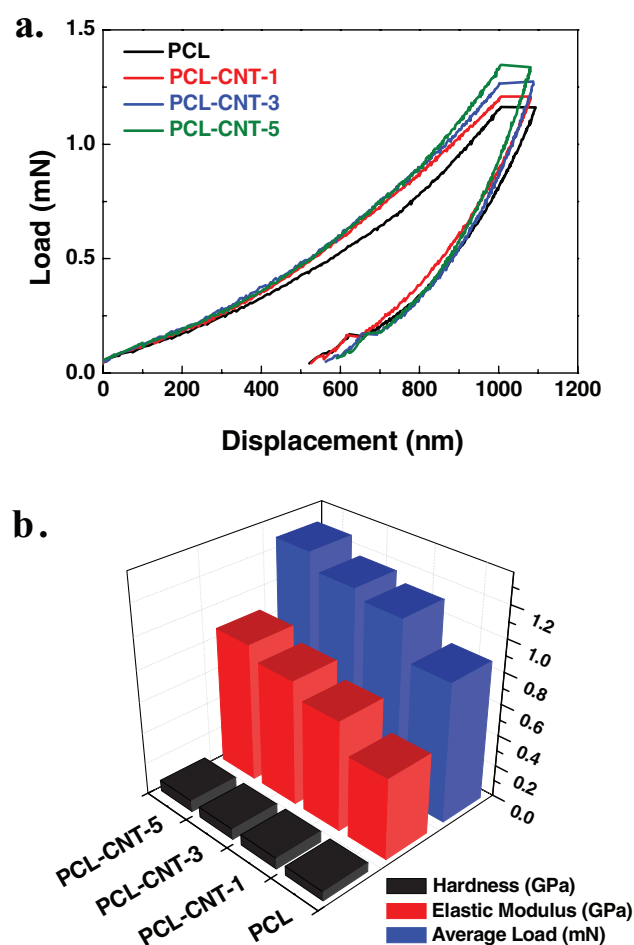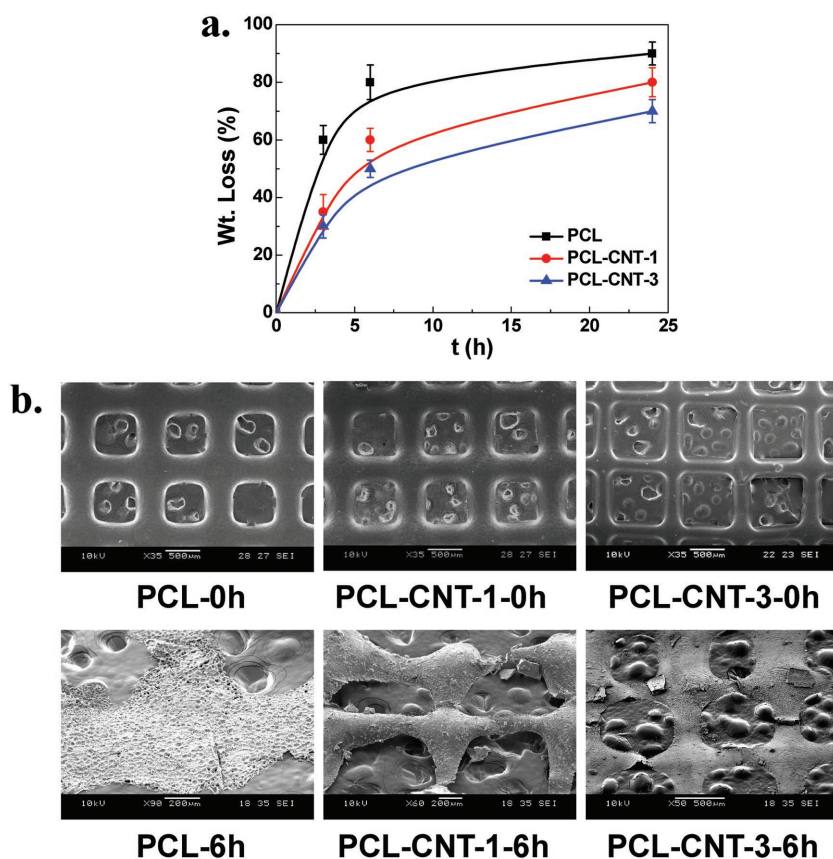

is fully recovered for PCL and its nanocomposites during unloading, demonstrating the elastic behavior of PCL and its nanocomposites even after the incorporation of CNTs. The lower indentation depth with the higher peak load is being observed with increasing CNT content in the nanocomposites. It is probably due to the increase in strength achieved via CNT reinforcement which resists the elastic deformation of the nanocomposites. The representative curve of different samples with maximum load value has been shown in Figure 5a. The maximum peak load value is 1.16, 1.21, 1.27, and 1.34 mN for PCL, PCL-CNT-1, PCL-CNT-3, and PCL-CNT-5, respectively, while the calculated average load value is 0.88 ± 0.28, 1.12 ± 0.09, 1.17 ± 0.10, and 1.27 ± 0.07 mN for PCL, PCL-CNT-1, PCL-CNT-3, and PCL-CNT-5, respectively (Figure 5b). The average load value and maximum peak load value gradually increase with increasing CNT content is because of the reinforcement effect of stiffer CNTs in the PCL matrix.

The elastic modulus (E) of PCL and its nanocomposites is being calculated by PCL-CNT-5 nanocomposite has an average value of 0.87 ± 0.10 GPa, which is a 70% improvement over PCL ($E = 0.51 \pm 0.18$ GPa). PCL-CNT-1 and PCL CNT-3 also show improvement of 35% and 55% in the E value, respectively, as compared to PCL. PCL-CNT-1 and PCL-CNT-3 have average E values of 0.69 ± 0.15 and 0.79 ± 0.06 GPa, respectively. The average E value of PCL-CNT-5 nanocomposite is slightly higher than PCL-CNT-1 and PCL-CNT-3. Similarly, hardness is also being calculated for PCL and its nanocomposites. The value of hardness is 0.057 ± 0.010, 0.069 ± 0.010, 0.067 ± 0.004, and 0.072 ± 0.003 GPa for PCL, PCL-CNT-1, PCL-CNT-3, and PCL-CNT-5, respectively. The increase in hardness can be explained by the reinforcement of CNT in PCL matrix with its increasing content. Thus the elastic modulus, peak load value, and hardness increase with increasing CNT content.

Conductivity of PCL-CNT nanocomposites increases with increasing CNT content. The conductivity value of PCL[50] is less than 10^{-15} S cm^{-1}, which increases six orders of magnitude for PCL-CNT-1. Eight and nine orders increase in the conductivity is being discerned for PCL-CNT-3 (2.2×10^{-7} S cm^{-1}) and PCL-CNT-5 (1.2×10^{-6} S cm^{-1}), respectively.

3.5. Enzymatic Biodegradation

Biodegradation studies[32,51,52] have been carried out on PCL and its nanocomposites at 37 °C in Pseudomonas lipase type XIII enzyme media in buffer solution shown in Figure 6a. The enzyme degradation rates of nanocomposites are slower as compared to pristine PCL. The weight loss of 70% and 80% has been observed for PCL-CNT-3 and PCL-CNT-1 scaffold, respectively, after 24 h of enzymatic degradation against the maximum weight loss for pure PCL. The PCL exhibits the faster degradation rate

Figure 5. Nanoindentation of PCL and its indicated nanocomposites. a) Representative maximum load versus displacement graph. b) Bar graph representing the comparison of hardness, modulus, and average load.

www.MaterialsViews.com

Early View Publication; these are NOT the final page numbers, use DOI for citation !!

Figure 6. a) Percentage weight loss of PCL and its indicated nanocomposite scaffolds during enzymatic (lipase from Pseudomonas sp., Type XIII) degradation at 37 °C. b) SEM images of PCL and its indicated nanocomposites before and after degradation. The "o h" and "6 h" indicate the time before and after 6 h degradation, respectively.

as compared to nanocomposites due to greater amorphous zone as compared to the nanocomposites, which are more susceptible to hydrolysis by enzymatic biodegradation. The morphology observed in SEM images of PCL and its CNT nanocomposites have been presented in Figure 6b to compare the degradation rates. The degradation images of scaffolds have been taken after 6 h. PCL and its nanocomposite scaffold having six grid windows for each sample is being displayed by SEM images at time *t* = 0. As it is discernible from the SEM images after 6 h, highest degradation is being observed for PCL followed by PCL-CNT-1 and PCL-CNT-3. Morphology of PCL and its nanocomposites cannot be observed after 24 h because it was difficult to recover the samples from the enzyme solution. The degradation rate is dependent on surface area and scaffold structure. In the case of grids the effective area and window pores enhance the binding activity and sites for Pseudomonas enzyme, which results in the higher and faster rate of biodegradation. However, enzymatic biodegradation of PCL and its nanocomposites can be tuned by varying the CNT percentage in the nanocomposites as well as the concentration of enzymes.
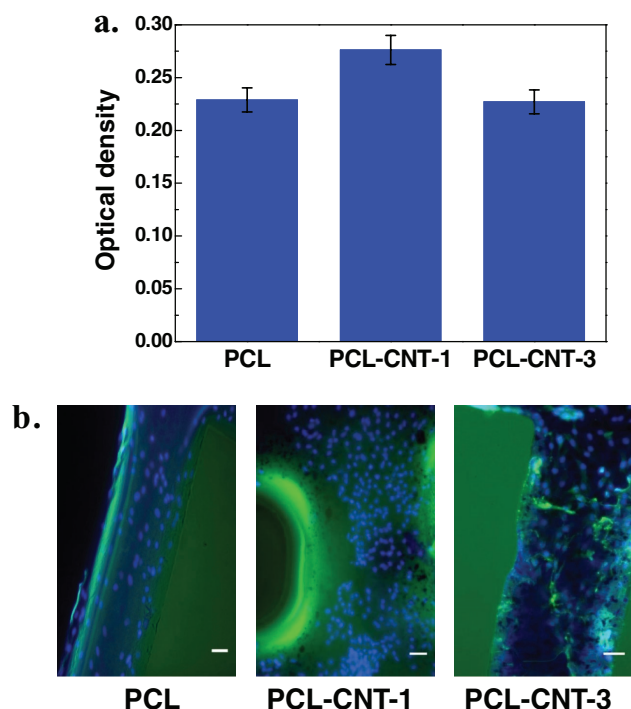
3.6. Cytotoxicity Assay and Cell Compatibility

MTT assay was performed to evaluate both the viability and toxicity of H9c2 mouse myoblast cells on PCL and its nanocomposite scaffolds for 4 d as shown in Figure 7a. MTT assay showed that cells were not only viable on PCL scaffold but also on the PCL-CNT nanocomposite as well. Based on this experimental condition, it seems that H9c2 cells on the PCL-CNT-1 scaffold have a greater proliferation than those growing on the PCL or PCL-CNT-3 scaffold. However, statistical analysis of the data showed that there is no significant difference in compare with the control indicating that the scaffolds may provide more favorable conditions for the adhesion and proliferations for the H9c2 cells. One major concern with the use of CNTs is toxicity to the cells.[53] Moreover, the cell scaffold fluorescence images were also captured to observe the cell growth and health after 4 d; cells are adhered on the surface of scaffolds and were growing in a healthier way. The cell proliferation was observed in all the scaffolds but was more in PCL-CNT-1 as compared to other scaffolds (Figure 7b). Additional assay of the PCL–CNT scaffolds using Live/dead staining assay for 4 d shown in Figure 8 was performed to show that cells were growing healthy with both PCL and its nanocomposites. Although it has been mentioned that CNT improves the proliferation of the cells,[53] it was observed in other cells types like L929 and NIH3T3 cells in PCL matrix.[51] The slight increase in proliferation of H9c2 myoblast cells on PCL-CNT nanocomposites was observed. No cytotoxic effect on H9c2 myoblast cells due to added CNTs was shown after several days in the printed PCL–CNT scaffolds.

4. Conclusions

Fabrication of well-defined PCL and its CNT composite scaffold structures was achieved by 3D printing. Incorporation of CNTs reinforced the alignment of the polymer chains resulting in slight enhancement in crystallinity and interaction with PCL matrix, which was observed from DSC and Raman spectroscopy. Nanoindentation results have shown the gradual enhancement in elastic modulus, hardness, and maximum peak load in PCL-CNT composites.

Early View Publication; these are NOT the final page numbers, use DOI for citation !!

a.

b.

PCL   PCL-CNT-1   PCL-CNT-3

Figure 7. a) MTT assay of H9c2 myoblast cells in PCL and its indicated nanocomposite scaffolds (unpaired *t*-test $P < 0.05$). b) Fluorescence images of H9c2 myoblast cells obtained through dye staining after 4 d of growth on PCL, PCL-CNT-1, and PCL-CNT-3 scaffolds (scale bar: 100 μm).

(a)   (b)

Control   PCL

(c)   (d)
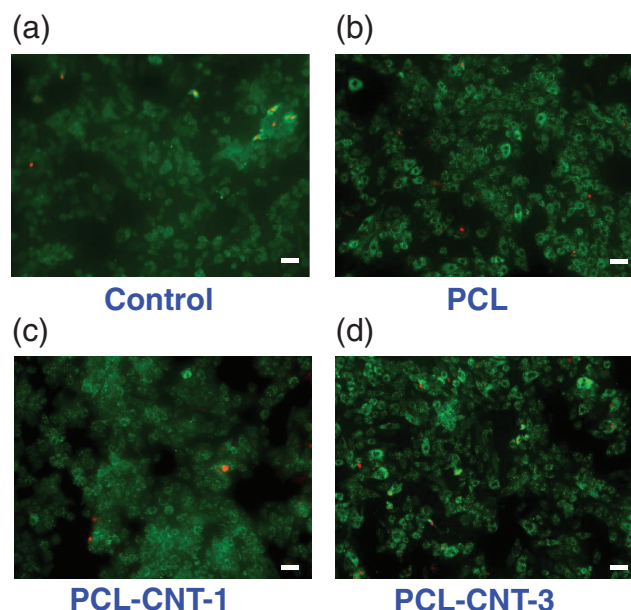
PCL-CNT-1   PCL-CNT-3

Figure 8. Fluorescence images of live (green) and dead (red) H9c2 myoblast cells obtained through dye staining after 3 d of growth on a) control, b) PCL, c) PCL-CNT-1, and d) PCL-CNT-3 scaffolds. Results show all scaffold was able to support growth of H9c2 cells. All the images are at a magnification of 10× (scale bar: 100 μm).

Enzymatic biodegradation revealed the structural and nanotube content dependence on the rate of biodegradation. Biodegradation can be tuned by selecting particular scaffold structure followed by the CNT content and enzyme concentration. MTT assay and fluorescence imaging results have shown that the myoblast cells are attaching to the scaffolds and are in healthy condition after 4 d. It can be concluded that PCL-CNT nanocomposites with 1% CNT show the optimal conductivity and stiffness for the proliferation of H9c2 cells. To conclude, PCL scaffolds have been fabricated with different CNT content using the 3D printer. Tuned degradation and cell compatibility might be further utilized for the application of the scaffolds in tissue engineering, as the PCL-CNT matrix can be enzymatically biodegraded after the formation of cardiac tissue.

Supporting Information

Supporting Information is available from the Wiley Online Library or from the author.

[1] S. Levenberg, R. Langer, *Curr. Top. Dev. Biol.* **2004**, *61*, 113.
[2] R. Langer, J. Vacanti, *Science* **1993**, *260*, 920.
[3] Q. L. Loh, C. Choong, *Tissue Eng., Part B* **2013**, *19*, 485.
[4] R. R. Jose, M. J. Rodriguez, T. A. Dixon, F. G. Omenetto, D. L. Kaplan, *ACS Biomater. Sci. Eng.* **2016**, *2*, 1662.
[5] R. R. Jose, J. E. Brown, K. E. Polido, F. G. Omenetto, D. L. Kaplan, *ACS Biomater. Sci. Eng.* **2015**, *1*, 780.
[6] A. Lendlein, R. Langer, *Science* **2002**, *296*, 1673.
[7] R. E. Drumright, P. R. Gruber, D. E. Henton, *Adv. Mater.* **2000**, *12*, 1841.
[8] A. G. Mikos, M. D. Lyman, L. E. Freed, R. Langer, *Biomaterials* **1994**, *15*, 55.
[9] A. J. Teo, A. Mishra, I. Park, Y.-J. Kim, W.-T. Park, Y.-J. Yoon, *ACS Biomater. Sci. Eng.* **2016**, *2*, 454.
[10] A.-V. Do, B. Khorsand, S. M. Geary, A. K. Salem, *Adv. Healthcare Mater.* **2015**, *4*, 1742.
[11] Y. J. Tan, W. Y. Yeong, X. Tan, J. An, K. S. Chian, K. F. Leong, *J. Mech. Behav. Biomed. Mater.* **2016**, *57*, 246.

Early View Publication; these are NOT the final page numbers, use DOI for citation !!

[12] H. Kweon, M. K. Yoo, I. K. Park, T. H. Kim, H. C. Lee, H.-S. Lee, J.-S. Oh, T. Akaike, C.-S. Cho, *Biomaterials* **2003**, *24*, 801.

[13] J. D. Erndt-Marino, D. J. Munoz-Pinto, S. Samavedi, A. C. Jimenez-Vergara, P. Diaz-Rodriguez, L. Woodard, D. Zhang, M. A. Grunlan, M. S. Hahn, *ACS Biomater. Sci. Eng.* **2015**, *1*, 1220.

[14] K. Uto, S. S. Mano, T. Aoyagi, M. Ebara, *ACS Biomater. Sci. Eng.* **2016**, *2*, 446.

[15] M. Khan, Z. Y. Ong, N. Wiradharma, A. B. E. Attia, Y.-Y. Yang, *Adv. Healthc. Mater.* **2012**, *1*, 373.

[16] W. Y. Yeong, N. Sudarmadji, H. Y. Yu, C. K. Chua, K. F. Leong, S. S. Venkatraman, Y. C. F. Boey, L. P. Tan, *Acta Biomater.* **2010**, *6*, 2028.

[17] T. Patrício, M. Domingos, A. Gloria, P. Bártolo, *Procedia CIRP* **2013**, *5*, 110.

[18] G. Nitya, G. T. Nair, U. Mony, K. P. Chennazhi, S. V. Nair, *J. Mater. Sci.: Mater. Med.* **2012**, *23*, 1749.

[19] W. Chaoying, C. Biqiong, *Biomed. Mater.* **2011**, *6*, 055010.

[20] S. H. Ku, M. Lee, C. B. Park, *Adv. Healthcare Mater.* **2013**, *2*, 244.

[21] K. Saeed, S.-Y. Park, H.-J. Lee, J.-B. Baek, W.-S. Huh, *Polymer* **2006**, *47*, 8019.

[22] K. Saeed, S. Y. Park, *J Appl. Polym. Sci.* **2007**, *104*, 1957.

[23] A. Mishra, B. P. D. Purkayastha, J. K. Roy, V. K. Aswal, P. Maiti, *Macromolecules* **2010**, *43*, 9928.

[24] A. Mishra, B. P. D. Purkayastha, J. K. Roy, V. K. Aswal, P. Maiti, *J. Phys. Chem. C* **2012**, *116*, 2260.

[25] W. Wang, R. A. Siegel, C. Wang, *ACS Biomater. Sci. Eng.* **2016**, *2*, 180.

[26] N. G. Sahoo, S. Rana, J. W. Cho, L. Li, S. H. Chan, *Prog. Polym. Sci.* **2010**, *35*, 837.

[27] S. E. Senyo, R. T. Lee, B. Kühn, *Stem Cell Res.* **2014**, *13*, 532.

[28] G. Vunjak-Novakovic, N. Tandon, A. Godier, R. Maidhof, A. Marsano, T. P. Martens, M. Radisic, *Tissue Eng., Part B* **2009**, *16*, 169.

[29] G. Marchioli, A. D. Luca, E. deKoning, M. Engelse, C. A. Van Blitterswijk, M. Karperien, A. A. Van Apeldoorn, L. Moroni, *Adv. Healthcare Mater.* **2016**, *5*, 1606.

[30] T. Xu, J. M. Miszuk, Y. Zhao, H. Sun, H. Fong, *Adv. Healthcare Mater.* **2015**, *4*, 2238.

[31] P. Pötschke, T. Villmow, B. Krause, *Polymer* **2013**, *54*, 3071.

[32] N. K. Singh, S. K. Singh, D. Dash, P. Gonugunta, M. Misra, P. Maiti, *J. Phys. Chem. C* **2013**, *117*, 10163.

[33] S. Sayyar, E. Murray, B. C. Thompson, S. Gambhir, D. L. Officer, G. G. Wallace, *Carbon* **2013**, *52*, 296.

[34] K. K. Gupta, A. Kundan, P. K. Mishra, P. Srivastava, S. Mohanty, N. K. Singh, A. Mishra, P. Maiti, *Phys. Chem. Chem. Phys.* **2012**, *14*, 12844.

[35] C. M. B. Ho, S. H. Ng, K. H. H. Li, Y.-J. Yoon, *Lab Chip* **2015**, *15*, 3627.

[36] C. M. B. Ho, S. H. Ng, Y.-J. Yoon, *Int. J. Precis. Eng. Manuf.* **2015**, *16*, 1035.

[37] J. M. Lee, W. Y. Yeong, *Virtual Phys. Prototyp.* **2015**, *10*, 3.

[38] R. Bhuthalingam, P. Q. Lim, S. A. Irvine, A. Agrawal, P. S. Mhaisalkar, J. An, C. K. Chua, S. Venkatraman, *Int. J. Bioprinting* **2015**, *1*, 57.

[39] J. E. Trachtenberg, J. K. Placone, B. T. Smith, C. M. Piard, M. Santoro, D. W. Scott, J. P. Fisher, A. G. Mikos, *ACS Biomater. Sci. Eng.* **2016**, *2*, 1771.

[40] J. E. Trachtenberg, P. M. Mountziaris, J. S. Miller, M. Wettergreen, F. K. Kasper, A. G. Mikos, *J. Biomed. Mater. Res., Part A* **2014**, *102*, 4326.

[41] M. Mattioli-Belmonte, G. Vozzi, Y. Whulanza, M. Seggiani, V. Fantauzzi, G. Orsini, A. Ahluwalia, *Mater. Sci. Eng., C* **2012**, *32*, 152.

[42] L. Liu, X. Wang, *Int. J. Bioprinting* **2015**, *1*, 77.

[43] G. Kister, G. Cassanas, M. Bergounhon, D. Hoarau, M. Vert, *Polymer* **2000**, *41*, 925.

[44] O. Hartman, C. Zhang, E. L. Adams, M. C. Farach-Carson, N. J. Petrelli, B. D. Chase, J. F. Rabolt, *Biomaterials* **2010**, *31*, 5700.

[45] A. Mishra, V. K. Aswal, P. Maiti, *J. Phys. Chem. B* **2010**, *114*, 5292.

[46] A. Bello, E. Laredo, J. R. Marval, M. Grimau, M. L. Arnal, A. J. Müller, B. Ruelle, P. Dubois, *Macromolecules* **2011**, *44*, 2819.

[47] D. Lahiri, F. Rouzaud, S. Namin, A. Keshri, J. Valdes, L. Kos, N. Tsoukias, A. Agarwal, *ACS Appl. Mater. Interfaces* **2009**, *1*, 2470.

[48] W. C. Oliver, G. M. Pharr, *J. Mater. Res.* **1992**, *7*, 1564.

[49] W. Channuan, J. Siripitayananon, R. Molloy, M. Sriyai, F. J. Davis, G. R. Mitchell, *Polymer* **2005**, *46*, 6411.

[50] S. J. Chin, P. Hornsby, D. Vengust, D. Mihailović, J. Mitra, P. Dawson, T. McNally, *Polym. Adv. Technol.* **2012**, *23*, 149.

[51] Z. Meng, W. Zheng, L. Li, Y. Zheng, *Mater. Sci. Eng., C* **2010**, *30*, 1014.

[52] N. K. Singh, B. D. Purkayastha, J. K. Roy, R. M. Banik, M. Yashpal, G. Singh, S. Malik, P. Maiti, *ACS Appl. Mater. Interfaces* **2010**, *2*, 69.

[53] J.-R. Lee, S. Ryu, S. Kim, B.-S. Kim, *Biomater. Res.* **2015**, *19*, 1.

Materials Views
www.MaterialsViews.com

Macromol. Biosci. **2016**, DOI: 10.1002/mabi.201600250
© 2016 WILEY-VCH Verlag GmbH & Co. KGaA, Weinheim

Macromolecular
Journals

9

Early View Publication; these are NOT the final page numbers, use DOI for citation !!